JCIS Open 8 (2022) 100066

Contents lists available at ScienceDirect

JCIS Open

journal homepage: www.journals.elsevier.com/jcis-open

Waterborne phenolic, triazine-based porous polymer particles for the removal of toxic metal ions

Konstantin B.L. Borchert [a], Robert Frenzel [a,b], Niklas Gerlach [a], Berthold Reis [a], Christine Steinbach [a], Benjamin Kohn [a], Ulrich Scheler [a], Simona Schwarz [a,*], Dana Schwarz [a,**]

[a] Leibniz-Institut für Polymerforschung Dresden e. V., Hohe Straße 6, 01069, Dresden, Germany
[b] Technische Universität Chemnitz, Straße der Nationen 62, 09111, Chemnitz, Germany

ARTICLE INFO

Keywords:
Triazine-based porous polymers
Waterborne colloidal synthesis
Cross-linked polymer
Adsorption
Water purification

ABSTRACT

Highly functional and also highly porous materials are presenting great advantages for applications in energy storage, catalysis and separation processes, which is why a continuous development of new materials can be seen. To create a material combining the promising potential interactions of triazine groups with the electrostatic or hydrogen bonding interactions of phenolic groups, a completely new polymeric resin was synthesized. From an eco-friendly dispersion polymerization in water, a copolymer network was obtained, which includes nine hydroxyl groups and one *s*-triazine ring per repetition unit. The polymer forms highly porous particles with specific surface areas up to 531 m^2/g and a negative streaming potential over a great pH range. The adsorption isotherms of Ni^{2+}, Cd^{2+}, and Pb^{2+} were studied in more detail achieving very good adsorption capacities (16 mg Ni^{2+}/g, 24 mg Cd^{2+}/g, and 90 mg Pb^{2+}/g). Demonstrating excellent properties for adsorption applications. The adsorbent exhibited selectivity for the adsorption of Pb^{2+} over more commonly occurring but non-toxic metal ions such as Fe^{2+}, Ca^{2+}, Mg^{2+}, and K^{+}. Furthermore, reusability of the material was demonstrated by facile, quantitative desorption of adsorbed Pb^{2+} with a small amount of diluted HCl, circumventing organic chelators. Subsequently, adsorption was carried out without decrease in adsorption performance.

1. Introduction

Highly functional materials based on cross-linked polymer networks are gaining immense attention due to their high stability and the facile introduction of various functional groups into their structure [1,2]. Especially triazine-based network structures such as triazine-based covalent frameworks have been investigated for different applications as gas capture and separation [3–8], catalysis [9,10] and various energy storage related applications [11,12]. Rather less frequently, triazine-based organic polymers are also investigated for their adsorption properties for aqueous pollutants for water treatment applications [13–18] although these polymers show great potential for separation technologies. It is also known that the triazine moiety itself is available to undergo various additional interactions [19], thus enhancing the adsorption capacities as it was shown e.g. for Cu^{2+} [14]. Part of our author team recently showed the viability of poly(melamine-co-formaldehyde) that is also featuring a triazine moiety, for the removal of various pollutants such as oxyanions, and organic pollutants and less frequently also heavy metal ions [16–18,20,21].

However, ion exchange resins are the material commonly used for the removal of aqueous pollutants as heavy metal ions at the moment [22–24]. Here, besides amino-functionalized resins [24–27], also phenolic resins are partially applied [28–32]. Ion exchange resins have various disadvantages as they tend to be expensive [33,34], partially lack a high removal efficiency [34] and are often synthesized using several organic solvents that partially neglects their ecological contribution. Using electrostatic interactions to achieve very good removal efficiency and high adsorption capacities for heavy metal ions is well-known from different polymeric or hybrid adsorbent materials with negatively charged groups such as hydroxyl, carboxyl, and phenolic groups [35–39].

Thus, the combination of negatively charged groups together with the before-mentioned enhancement from the triazine moieties presents a great potential for efficient adsorption of heavy metal ions in realistically low concentrations. Although the synthesis of these kind of polymers

* Corresponding author.
** Corresponding author.
E-mail addresses: borchert@ipfdd.de (K.B.L. Borchert), frenzel-robert@ipfdd.de (R. Frenzel), gerlach@ipfdd.de (N. Gerlach), reis@ipfdd.de (B. Reis), steinbach@ipfdd.de (C. Steinbach), kohn@ipfdd.de (B. Kohn), scheler@ipfdd.de (U. Scheler), simsch@ipfdd.de (S. Schwarz), schwarz-dana@ipfdd.de (D. Schwarz).

https://doi.org/10.1016/j.jciso.2022.100066
Received 10 June 2022; Received in revised form 13 October 2022; Accepted 2 November 2022

have seldom been reported [3,11,40], only Gómez-Ceballos et al. applied such material, a hyperbranched polymer network from oxidized lignin and cyanuric chloride, for heavy metal adsorption [40]. Nandi et al. used monomers, which are comprised of an *s*-triazine ring with three moieties of resorcinol or phloroglucinol, which were cross-linked with terephthalaldehyde and used as solid electrolyte. The comprising functional hydroxyl and *s*-triazine groups also pose a really viable starting point for the application as potential adsorbents [11].

The phloroglucinol-based monomer (shown in Fig. 1) includes nine hydroxyl groups per *s*-triazine monomer that should enable strong interactions with metal ions. This monomer was also reported for its strong intermolecular hydrogen bonds of the hydroxyl proton to the *s*-triazine nitrogen [41], showing potential synergistic effects for adsorption interactions. Nandi et al. showed the polymerization of this monomer to obtain a highly nanoporous and highly functional polymer particles that should also add to their adsorption efficiency. However, the synthesis of the monomer together with terephthalaldehyde as cross-linker uses harsh hydrothermal conditions in organic solvents such as dioxane, tetrahydrofuran and includes washing with dimethyl formamide. This partly diminishes a potential use for environmental applications. In literature, many examples can be found for adsorbents with proposed environmental applications, which are synthesized using large amounts of surfactants, energy or organic solvents as e.g. dimethyl sulfoxide. In these, often contaminations with the surfactant [18] or residuals from the solvent can be found [42,43]. Therefore, we planned a more eco-friendly polymerization route, which only includes water as solvent and that uses no catalyst (see Fig. 1).

Here, we present the facile synthesis of a new copolymer with an extremely high number of phenolic groups in a triazine-based polymer. It can be obtained by an eco-friendly, catalyst-free dispersion polymerization with water as solvent. By variation of the amount of formaldehyde as cross-linker, particles with different porosities were achieved. We thoroughly characterized the obtained particles using N_2 and CO_2 adsorption, electron microscopy, ATR-FTIR, elemental analysis, and thermogravimetric analysis. As a colloidal approach was used for the preparation, the synthesis of the polymer is easily upscaleable without impaired morphological or chemical properties. To demonstrate a potential application for the particles, adsorption isotherms with lead, cadmium, and nickel ions as pollutants in water were investigated. These ions are posing a great risk to aquatic organisms as well as humans [44–51], thus complete removal is critical.

2. Materials and methods

2.1. Materials

2.1.1. Chemicals used for the synthesis

Aluminum(III) chloride (anhydrous, ≥ 99%), cyanuric chloride (anhydrous, ≥ 99%), paraformaldehyde (F) (≥95%), and phloroglucinol (1,3,5-trihydroxybenzene, ≥ 99%) were purchased from Sigma-Aldrich (Merck KGaA, Darmstadt, Germany). Anhydrous solvents dichloromethane (DCM) and diethyl ether (Et_2O) were purchased from Carl Roth (Karlsruhe, Germany). Hydrochloric acid (37 wt%, Normapure) and ethanol (absolute, Normapur) were purchased from VWR International (Darmstadt, Germany). NaOH (≥98%, p.a.) was purchased from Honeywell (Offenbach, Germany). All listed chemicals were used without further purification.

2.1.2. ICP-OES standard solutions

For the preparation of the elemental standards for ICP-OES analysis,

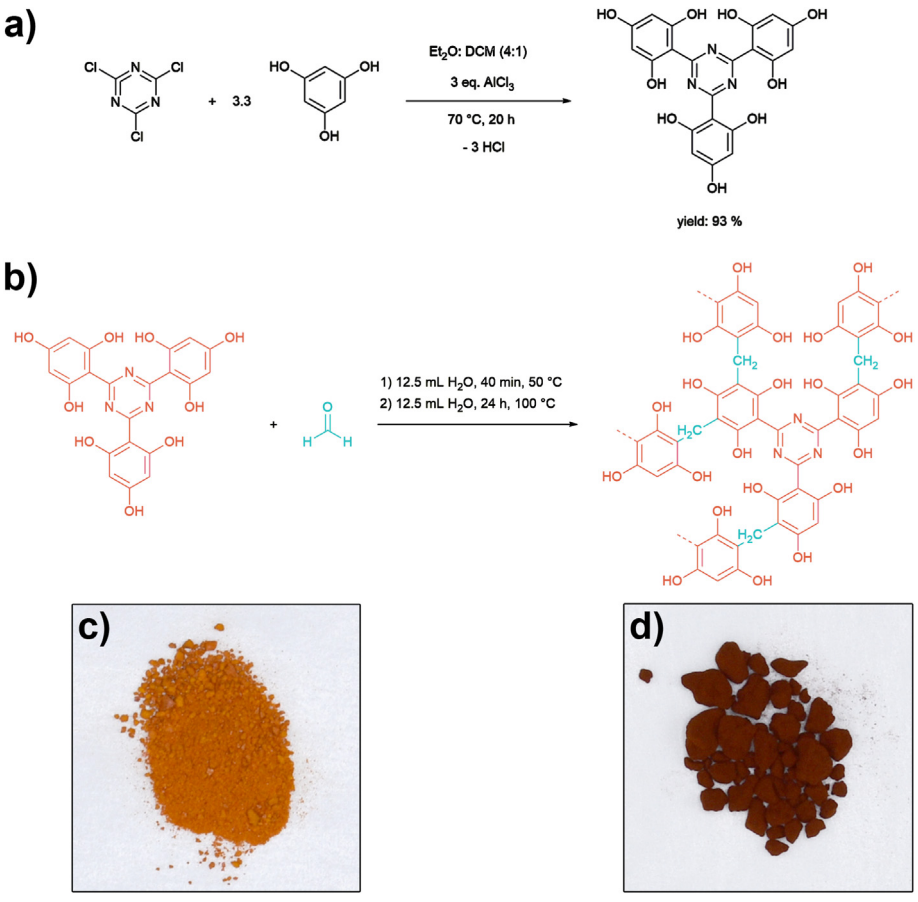

Fig. 1. a) Synthesis of the monomer 3PT [41], b) reaction scheme of the synthesis of poly(3PT-*co*-formaldehyde) (P(3PT-F)), c) Image of 3PT powder, and d) image of P(3PT-F)-3L.

the following standards were used: 9998 mg/L S in water (Sigma Aldrich, München, Germany), 10008 mg/L Pb in water (Sigma Aldrich, München, Germany), 10000 mg/L Ni in 2 mol/L HNO_3 (Bernd Kraft, Duisburg, Germany), and 10000 mg/L Cd in 2 mol/L HNO_3 (Bernd Kraft, Duisburg, Germany). For the selectivity experiments, the ICP multi-element standard solution IV (Merck KGaA, Certipur®) was used. Nitric acid (65 wt%, p.a.) purchased from VWR International (Darmstadt, Germany) was used for preparing the matrix.

2.1.3. Ultrapure water

As medium for adsorption experiments, reactions, and ICP-OES standards, ultrapure water purified by a Milli-Q Advantage A10® system (TOC 5 ppb, resistivity of 18.2 MΩ cm at 25 °C) was used.

2.1.4. Chemicals used for the adsorption process

Cadmium(II) sulfate octahydrate (p.a.) and magnesium chloride (anhydrous, for synthesis) were purchased from Merck KGaA (Darmstadt, Germany). Lead(II) nitrate (99.999%), nickel(II) sulfate hexahydrate (≥98%), iron(II) chloride tetrahydrate (ReagentPlus®), potassium chloride (p.a.), and copper(II) chloride dihydrate (reagent grade) were purchased from Sigma-Aldrich (Merck KGaA, Darmstadt, Germany). Lead(II) chloride (98%) was purchased from Aldrich (Merck KGaA, Darmstadt, Germany). Calcium chloride (anhydrous, ≥ 94%) was purchased from Carl Roth (Karlsruhe, Germany). All listed chemicals were used without further purification.

2.2. Synthesis

2.2.1. Synthesis of 2,4,6-tris(2,4,6-trihydroxyphenyl)-1,3,5-triazine (3PT)

The synthesis of the monomer 2,4,6-tris(2,4,6-trihydroxyphenyl)-1,3,5-triazine (3PT) was carried out in a Friedel-Crafts arylation according to Conn and Eisler with some adjustments (Fig. 1) [41]. The synthesis and handling of air and moisture sensitive chemicals was carried out under inert gas atmosphere (nitrogen) using common Schlenk techniques to prevent reactions with oxygen and water for example.

Starting with a three-necked round bottom flask (1000 mL) with attached reflux condenser, dropping funnel and a stir bar, cyanuric chloride (8.29 g, 45.0 mmol, 1.0 eq.) and phloroglucinol (18.80 g, 149.1 mmol, 3.3 eq.) were added to the reaction vessel under inert gas counterflow. The solids were suspended in ether (300 mL) and DCM (100 mL). In a second round bottom flask (250 mL) $AlCl_3$ (17.80 g, 133.5 mmol, 2.96 eq.) was dissolved in ether (100 mL) at 0 °C. The rose-tinted $AlCl_3$ solution was transferred to a dropping funnel and slowly added to the ice-cooled suspension over the course of 30 min under intense stirring. The suspended solids dissolved in the mixture and a color change from pale yellow to a bright orange were observed. After the addition was completed, the reaction mixture was left for stirring until room temperature was reached. Subsequently, the mixture was heated to 70 °C for 20 h under reflux. During this period, the solution changed color once again to a deep red. After the mixture reached room temperature again, ethanol (50 mL) was added. The orange precipitate was filtrated with a fritted glass (POR 4), washed thoroughly with ether, and finally dried at 100 °C for 24 h. For further purification, the crude product was suspended in hydrochloric acid (10 %, 300 mL). The suspension was centrifuged at 5000 rpm for 5 min. This purification procedure was repeated with $HCl_{(aq)}$, ultrapure water, and ether. Finally, the solid was filtrated through a fritted glass (POR 3). Residual solvent was removed via vacuum drying at 100 °C for 48 h. The synthesis yielded in 19.0 g (41.8 mmol, corresponding to 93 % in relation to cyanuric chloride) bright orange powder.

Elemental analysis *(theoretical values given in brackets)*: $C_{21}H_{15}N_3O_9$, C: 50.17 wt% *(55.64 wt%)*, H: 4.22 wt% *(3.34 wt%)*, N: 8.39 wt% *(9.27 wt%)*. C/N-ratio (mol/mol): 6.97 *(7.00)*.

^{1}H-NMR: δ = 5.90 ppm (s, 6H, aryl-H), 10.10 ppm (s_{br}, 3H, *p*-OH), 12.25 ppm (s_{br}, 6H, *o*-OH)

^{13}C-NMR: δ = 95.69 ppm (*3*-aryl-C and *5*-aryl-C), 98.95 ppm (*1*-aryl-C), 163.18 ppm (*2*-aryl-C and *6*-aryl-C), 163.85 ppm (*4*-aryl-C), and 166.62 ppm (*s*-triazine-C).

2.2.2. Synthesis of Poly(3PT-co-formaldehyde) with 1 eq. 3PT to 3 eq. formaldehyde (P(3PT-F)-3)

In a round bottom flask (100 mL) equipped with a stirring bar and a reflux condenser, 3PT (0.7 g, 1.54 mmol, 1 eq.) and paraformaldehyde (F, 139.08 mg, 4.63 mmol, 3 eq.) were suspended in ultrapure water (12.5 mL). The mixture was heated to 50 °C for 40 min under constant stirring. Afterwards, 12.5 mL ultrapure water was added and the temperature was raised to 100 °C. After 24 h under reflux and constant stirring, the suspension changed color from bright orange to carmine. The solid was filtered off with a fritted glass (POR 4), washed with ultrapure water and ethanol, and dried at 100 °C for 24 h. For additional purification, the raw product was treated with hot ethanol in a Soxhlet extractor for 72 h. Subsequently, the solid was dried at 100 °C for 24 h in an oven and another 24 h at 100 °C in a vacuum drying oven.

2.2.3. Synthesis of P(3PT-F)-2, P(3PT-F)-4 and P(3PT-F)-3L

Reactions with an alternation of the amount of paraformaldehyde were carried out. The procedure followed the already described procedure for the synthesis of P(3PT-F)-3 in section 2.2.1. For P(3PT-F)-2 and P(3PT-F)-4, the amounts of formaldehyde used in the synthesis were varied.

For the upscaled synthesis of P(3PT-F)-3L, the amounts of 3PT, F and water as dispersant were multiplied to the 2.85-fold amounts with respect to P(3PT-F)-3. All used amounts are also stated in Table 1.

2.3. Characterization

2.3.1. pH measurements

pH measurements were carried out with the device SevenExcellence pH/Ion/C/DO meter S975–K equipped with an InLab Expert Pro-2m-ISM electrode, both from Mettler Toledo, Gießen, Germany.

2.3.2. Scanning electron microscopy

Scanning electron microscopy (SEM) was performed to analyze the particles at nanometric scale (SEM Ultra plus, Carl Zeiss Microscopy GmbH, Oberkochen, Germany) using a secondary electron detector (SE2). Before each analysis, the samples were attached to an aluminum pin sample tray with double-sided adhesive carbon tape and coated with 3 nm platinum to avoid electrostatic charging.

2.3.3. Thermogravimetric analysis

Thermogravimetric analysis (TG) was performed by using the device 1 Star System from Mettler Toledo Gießen, Germany. The measurements were carried out with approximately 5–7 mg of the respective sample in a platinum crucible. The investigated temperature range was from 30 °C to 1000 °C with a heating rate of 10 °C/min under air atmosphere and under N_2 atmosphere, with a flow rate of 40 mL/min.

2.3.4. Nitrogen sorption

Nitrogen sorption measurements were performed using the Autosorb iQ MP from Quantachrome Instruments. The samples were dried in a

Table 1
Respective masses of the two monomers, 3PT and paraformaldehyde (F), and dispersant volumes used in the synthesis and variation of the equivalents of F for the products P(3PT-F)-2, P(3PT-F)-3, P(3PT-F)-4, and P(3PT-F)-3L.

Sample	Molar equivalents F:3PT	Mass 3PT in g	Mass F in mg	V water in mL
P(3PT-F)-2	2:1	0.7	93	12.5 + 12.5
P(3PT-F)-3	3:1	0.7	139	12.5 + 12.5
P(3PT-F)-4	4:1	0.7	185	12.5 + 12.5
P(3PT-F)-3L	3:1	2.0	400	35.5 + 35.5

vacuum oven at 120 °C and activated by degassing in vacuum ($5 \bullet 10^{-10}$ mbar) at 100 °C for 24 h. Approximately 50 mg of the polymer particles was used for the measurement. The N_2 sorption measurements were performed at 77 K. The specific surface area S_{BET} was calculated using the multi-point Brunauer-Emmet-Teller method [52–54]. The pore size distribution (PSD) was determined by a fitting with a quenched-solid density functional theory model (QSDFT) for adsorption of N_2 to carbon including slit, sphere, and cylindrical pores.

2.3.5. Carbon dioxide sorption

Carbon dioxide sorption measurements were performed using the Autosorb iQ MP from Quantachrome Instruments. The samples were dried in a vacuum oven at 90 °C and activated by degassing in vacuum ($5 \bullet 10^{-10}$ mbar) at 100 °C for 24 h. Approximately 70 mg of the polymer particles was used for the measurement. The CO_2 sorption measurements were performed at 273 K.

2.3.6. Inductively coupled plasma optical emission spectrometry

Inductively Coupled Plasma Optical Emission Spectrometry (ICP-OES) (iCAP 7400 from Thermo Scientific) was used to determine the heavy metal ion concentrations in simulated and real water. Thus, eight matrix-matched, external standard solutions were used for calibration, containing the analyzed elements (Ca, Mg, Fe, Ni, Cu, Cd, K, Pb, S) each in the same concentration (0.1 mg/L, 0.5 mg/L, 1 mg/L, 5 mg/L, 10 mg/L, 50 mg/L, 100 mg/L, or 500 mg/L, respectively). To each sample (8 mL), 2 mL 20% nitric acid was added prior to analysis. All samples were measured thrice.

2.3.7. UV–Vis spectroscopy

For the determination of the nitrate and chloride ion concentrations, the UV–Vis-spectrophotometer DR6000 (Hach Lange GmbH, Germany) was used with the associated Hach Lange cuvette test kits LCK 340 for nitrate (valid for a concentration range between 5 mg/L and 155 mg/L) and LCK 311 for chloride (valid for a concentration range between 1 mg/L and 1000 mg/L).

2.3.8. Attenuated total reflection infrared spectroscopy

Attenuated total reflection infrared spectroscopy (ATR-FTIR) measurements were preformed using a Tensor 27 device equipped with a Platinum ATR module both from Bruker Corporation, Billerica, USA. All samples were measured in dry state with a resolution of 2 cm^{-1} and with 100 scans under constant nitrogen flow to remove other atmospheric components. The acquired spectra were additionally subjected to an atmospheric compensation to remove the rotation bands of water.

2.3.9. Nuclear magnetic resonance

The monomer samples were dissolved in DMSO-d_6. ^{1}H- and $^{13}C\{^1H\}$-spectra were measured using an Avance III 500 MHz Bruker Biospin system (^{1}H NMR at 500.30 MHz, $^{13}C\{^1H\}$-NMR at 125.80 MHz). Measurements were carried out at 20 °C and atmospheric pressure. The signals of the protons and carbon atoms of the solvent DMSO- d_6 was used as an internal standard ($\delta_H = 2.50$ ppm, $\delta_C = 39.52$ ppm).

CP-MAS solid-state NMR experiments have been performed on a Bruker Avance III 300 NMR spectrometer using a HF/X BL 4 mm MAS probe head with a sample spinning frequency of 8 kHz. Cross polarization was performed with a 2 ms contact time and 4 s repetition time a total of 16384 scans. The ^{13}C chemical shift and Hartmann-Hahn match condition were adjusted with Adamantane and decoupling power was optimized with $^{13}C_2$ enriched Glycine.

2.3.10. Wide angle X-ray scattering (WAXS)

WAXS patterns were recorded using a Bruker D8 Discover diffractometer (Bruker, Karlsruhe, Germany) with a Cu Twist tube (λ = 0.154018 nm, operating at 40 kV and 40 mA) in reflection mode with a zero-background silicon specimen holder. The diffraction patterns were recorded with a VÅNTEC-500 2D detector using a sample-to-detector distance of 149.8 mm. The pattern of each sample (from 10° to 65°) was measured in two steps (step 1: $\Theta = 5°$, detector (middle) = 20°, $2\Theta = 25°$; step 2: $\Theta = 12.5°$, detector (middle) = 37.5°, $2\Theta = 50°$) with a detection time of 30 min/step. The diffraction patterns were integrated, combined, and then displayed as plot of the intensity as a function of 2Θ.

2.3.11. Particles size measurements

Particles sizes of the purified particles were analyzed using a Mastersizer Microplus (Malvern, Kassel Germany). For redispersion of the particles, 0.05 g of the sample was dispersed with ultrasonication in 10 mL ultrapure water. The resulting dispersion was then dropwise added to the measurement cell until the detector obscuration was between 13 and 20%. The data was evaluated using the model "Polydisperse", a particle refractive index (RI) of 1.5, absorbance of 0.01000 and a dispersant RI: 1.3300.

2.3.12. Streaming potential vs. pH measurements

Streaming potential vs. pH curves were measured to determine the surface charge of the particle in dependence of the pH. 0.1 g of the particles was redispersed using ultrasonication in 100 mL of ultrapure water. The resulting dispersion was characterized by titration to pH 9.0 from the initial pH of 3.5 with the particle charge detector Mütek PCD-04 from the company BTG Instruments GmbH, Wessling, Germany with 0.1 M NaOH, respectively.

2.3.13. Scanning electron microscope with energy-dispersive X-ray spectroscopy

Scanning electron microscope with energy-dispersive X-ray spectroscopy (SEM-EDX): The elemental mapping of the samples after adsorptions was carried out using a Phenom XL Workstation from Thermo Scientific (Waltham, USA) with an energy-dispersive X-ray spectroscopy detector (Silicon Drift Detector SDD, thermoelectrically cooled (LN2free), 25 mm^2 detector active area). The samples were fixed on a double-sided adhesive carbon tape on an aluminum pin sample tray. The measurements were carried out in low vacuum mode (p = 60 Pa) with an acceleration voltage of 10 keV at different magnifications.

2.3.14. Elemental analysis

Elemental analysis was carried out using a vario MICRO cube from the company Elementar, Langenselbold, Germany.

2.3.15. Centrifugation

The adsorbent material was separated from the supernatant by double centrifugation, each at 22,000×*g* for 8 min at r.t. with the device 3-18KS from Sigma Laborzentrifugen (Osterode am Harz, Germany).

2.4. Batch adsorption experiments

For all adsorption experiments, stock solutions of the respective heavy metal salt were prepared in a 500 mL volumetric flask to achieve the desired concentrations. Therefor, the salts were dissolved in water. The pH of the resulting solutions was not adjusted. 30 mg of the polymer particles was placed into a 50 mL poly(propylene) centrifuge tube. Subsequently, 30 mL of the respective heavy metal salt solution was added. The samples were stirred for 24 h at 23 °C with a magnetic stirrer. After centrifugation, the pH of the supernatant was analyzed. 8 mL of the supernatant was taken and mixed with 2 mL of 20 wt% nitric acid for ICP-OES analysis.

2.5. Adsorption experiments at varying pH_0

For experiments with varying pH_0 values, respective stock solutions of $Pb(NO_3)_2$ were adjusted in pH by dropwise addition of aqueous HNO_3 until the stated pH was achieved. The subsequent adsorption experiments were conducted as stated in section 2.4.

2.5.1. Selectivity experiments

For the selectivity experiments, a stock solution was prepared by dissolving 0.5 mmol of the following salts in 1 L ultrapure water: $PbCl_2$, $CuCl_2$, $FeCl_2$, $MgCl_2$, $CaCl_2$, and KCl. The adsorption experiment was carried out as triplet according to the procedure stated in section 2.4.

2.5.2. Recycling experiments with $HCl_{(aq)}$

To show the reusability, adsorption experiments with a $Pb(NO_3)_2$ solution of 100 mg/L Pb^{2+} was carried out as stated in section 2.4. After separation of the precipitate from the supernatant, the precipitate was rinsed twice with 2 mL of water. For desorption, 10 mL of 0.5 M aqueous HCl was added. The sample was shaken for 3 h and centrifuged afterwards. The supernatant was analyzed by ICP-OES to determine the amount desorbed. For the regeneration of the adsorbent, 10 mL 0.5 M HCl was again added to the samples with subsequent shaking for 3 h. Afterwards, a second adsorption was conducted with the sample in the same manner. The adsorption/desorption/adsorption experiment was conducted as duplet.

2.6. Calculation and theoretical models

The percentage adsorption of the samples in equilibrium was determined using Equation (1), whereby the initial concentrations c_0 and the equilibrium concentration c_{eq} were analyzed by ICP-OES:

$$\text{adsorption in } \% = 100\% \cdot \frac{c_0 - c_{eq}}{c_0} \tag{1}$$

The respective adsorption capacity q_{eq} was calculated as follows:

$$q_{eq} = \frac{(c_0 - c_{eq}) \cdot V_L}{m_A} \tag{2}$$

Here, V_L refers to the given volume of the adsorptive solution and m_A to the mass of the sorbent material used in the experiment. For desorption, the respective desorbed capacity was calculated as follows, whereby V_L is equal to the 10 mL which was used as solution volume for desorption and c_{eq} is the concentration of Pb^{2+} in solution after desorption:

$$q_{Des} = \frac{c_{eq} \cdot V_L}{m_A} \tag{3}$$

2.6.1. Isotherm models

To model the adsorption process mathematically, different isotherm models were fitted. We applied the non-linear models of the Langmuir [55], Sips [56] and Dubinin-Radushkevich [57] models as given in Equations (4)–(10).

Langmuir model:

$$q_{eq} = \frac{Q_m \cdot K_L \cdot c_{eq}}{1 + K_L \cdot c_{eq}} \tag{4}$$

Sips model:

$$q_{eq} = \frac{Q_m \cdot K_S \cdot c_{eq}^n}{1 + K_S \cdot c_{eq}^n} \tag{5}$$

K_L and K_S thereby represent the respective model equilibrium constants for Langmuir and Sips, Q_m the maximum adsorption capacity, n the Sips model exponent [58–60].

Dubinin-Radushkevich:

$$q_{eq} = Q_m \cdot \exp\left(-\beta_{DR} \cdot \left(RT \cdot \ln\left(1 + \frac{1}{c_{eq}}\right)\right)^2\right) \tag{6}$$

Equation (6) is the final non-linear form of the Dubinin-Radushkevich model that was used for fitting. It was modified in the following way. In Equation (7), the original form of the equation is displayed [57]. The Polanyi potential ε can further be expressed by Equation (8), whereby T is the given temperature and R the universal gas constant [58,59]. c_S refers to the saturation concentration. However, as the saturation concentration is not easily accessible for the given species in the present adsorption system, thus it cannot be modelled this way. As pointed out by Zhou [61], the term inside the logarithm can be exchanged for the same numerical solution as it is displayed in Equation (9) with two absolutely necessary requirements: First, the equilibrium concentrations needs to be much smaller than the saturation concentration ($c_{eq} \ll c_S$). Second, this substitution requirs mol/L as unit for the concentration. In the end, the combination of Equations 7 and 9 leads to Equation (6) that was then applied in the modelling.

$$q_{eq} = Q_m \cdot \exp\left(-\beta_{DR} \cdot \varepsilon^2\right) \tag{7}$$

$$\varepsilon = RT \cdot \ln\left(\frac{c_S}{c_{eq}}\right) \tag{8}$$

$$\varepsilon = RT \cdot \ln\left(1 + \frac{1}{c_{eq}}\right) \tag{9}$$

With these requirements, the energy of adsorption $E_{ads,DR}$ can be expressed by the relation to the activity coefficient β_{DR}, as given in Equation (10).

$$E_{ads,DR} = \frac{1}{\sqrt{2 \cdot \beta_{DR}}} \tag{10}$$

In general, non-linear fitting was performed because linearization is changing dependent and independent variables and their errors in an numerically unpredictable way as pointed out by literature [62–64]. The fitting was performed in Origin 2022 with the Levenberg-Marquardt algorithm until X^2 reached a value below 10^{-9} and did not change further.

3. Results and discussion

Highly functional polymer networks that include both phenolic and triazine groups, are promising materials for the removal of heavy metal ions from aqueous solutions. To study this approach, we synthesized a copolymer that has not been reported in literature, until now. Herein, we used a monomer which consists of three phloroglucinol groups bound to an *s*-triazine ring (3PT), known from literature [41]. In a dispersion polymerization in water, 3PT was polymerized with different amounts of paraformaldehyde (F) yielding in nanoporous polymeric particles (P(3PT-F)). To investigate the polymerization and particle formation mechanism, the P(3PT-F) particles were characterized toward their chemical composition, pore morphology and particle size. As application-oriented proof of concept, we scaled up the colloidal synthesis. Finally, the adsorption isotherms for Ni^{2+}, Cd^{2+}, and Pb^{2+} were acquired over a wide concentration range to determine the adsorption capacity.

3.1. Synthesis and characterization of the polymer particles

The monomer used, 3PT, was synthesized by a Friedel-Crafts arylation using $AlCl_3$ as catalyst according to the procedure reported by Conn and Eisler with minor modifications to improve the consistency in the catalyst addition step [41]. NMR and ATR-FTIR (see Fig. 5 and Figs. S1 and S2) proved the identity of the bright orange powder and TGA measurements (see Fig. S3) ensured the absence of residual aluminum species from the catalyst. In WAXS measurements, the monomer exhibited a strong but broad reflex at 26.6° and two minor, broad reflexes at 13.3° and 18.1° (see Fig. S9).

For the polymerization, the dissolution and homogenization of the educts was ensured in a first step at 50 °C for 40 min. Afterwards, the polymerization was conducted in the second step (100 °C, 24 h). We varied the equivalents of paraformaldehyde used as cross-linker with respect to the 3PT monomer with molar ratios of 1:2 for P(3PT-F)-2, 1:3

for P(3PT-F)-3 and 1:4 for P(3PT-F)-4. We obtained powdered products with intense, dark red color. First, N_2 and CO_2 sorption experiments were conducted to investigate the porosity of the obtained polymers (see Fig. 2 and Table 2). As it can be seen in the N_2 experiments, the samples P(3PT-F)-2, P(3PT-F)-3, and P(3PT-F)-4 exhibit a type IV(a) isotherm with H4 hysteresis loops [53,54,65].

This kind of isotherms is associated with materials incorporating both, micro- and mesopores. The uptake in the p/p_0 range below 0.1 show micropore condensation of N_2 while the hysteresis loop with the beginning at approximately $p/p_0 = 0.42$ is caused by the filling of the mesopores. The non-parallel shape of the hysteresis itself is due to a broad pore size distribution. The delayed adsorption and desorption here indicates pore blockage effects by broad variation in pore sizes and only partially filled macropores. The usage of three different cross-linker amounts affects the pore structure as it can be seen from variation in the specific surface area S_{BET} and the pore volume of the samples (see Table 2). From these three samples, P(3PT-F)-3 shows the highest specific surface area with 493 m^2/g. The use of less or more paraformaldehyde leads to a decrease of specific surface area that indicates an optimum at 3 equivalents in terms of cross-linking and the accessibility of the resulting pores especially in the microporous region. The pore size distribution (PSD) supports these findings (see Fig. 2b). First, micropores with diameters below 2 nm can be seen for all samples. Additionally, two broad peaks are visible in the mesoporous region with maxima approximately at 3.2 nm and 6.5 nm. A very slight shift to lower diameters in the maxima can be seen from P(3PT-F)-2 to P(3PT-F)-4.

It is important to note that for the application in adsorption processes, two main points are crucial: First, micropores add greatly to the specific surface area that is important to maximize the potential uptake of pollutants by maximizing the amount of accessible adsorption sides of the material. Secondly, mesopores are necessary to enhance the diffusion and mass transfer in the adsorption to shorten the time needed to reach the maximum uptake that can be expressed by the pore volume given in Table 2. With this in mind, P(3PT-F)-3 showed the best results of the three materials in terms of both, specific surface area and pore volume. For this reason we decided to conduct an enlarged synthesis approach analogues to P(3PT-F)-3 for a subsequent application in adsorption experiments that was labeled P(3PT-F)-3L. P(3PT-F)-3L showed a nitrogen sorption isotherm and PSD very similar to the ones of sample P(3PT-F)-3. However, from the enlarged scale of the synthesis, a higher specific surface area (531 m^2/g) and increased pore volume (0.56 cm^3/g) was obtained. Potentially the altered heating of the bigger reaction flask could have resulted in a decrease in initial polymerization rate leading to overall higher pore accessibility and higher specific surface area. The sorption measurements with carbon dioxide (CO_2) at 273 K show bent isotherms with hysteresis loops and confirms ultramicroporosity for all the samples (see Fig. S5).

In SEM images (Fig. 3) it can be seen that particles in the micrometer range were obtained. The single particles also show a tendency towards formation of larger aggregates in the case of P(3PT-F)-2 and P(3PT-F)-3. The particles of P(3PT-F)-2 show a polyhedral shape with smooth surfaces, while P(3PT-F)-3 exhibits a more flake-like surface morphology. In contrast, the particles of P(3PT-F)-4 are spherical with smooth surfaces again. P(3PT-F)-3L presents the same features and morphology as P(3PT-F)-3.

Table 2
Surface area (S_{BET}), pore volume (PV), and micro pore volume (MPV) of the samples. Carbon dioxide (CO_2) sorption isotherms measured at 273 K are shown in Fig. S5.

Sample code	S_{BET} [a] n m^2/g	PV [b] n cm^3/g	MPV [c] n cm^3/g
P(3PT-F)-2	395	0.40	0.15
P(3PT-F)-3	493	0.53	0.18
P(3PT-F)-4	464	0.45	0.17
P(3PT-F)-3L	531	0.56	0.20

[a] Surface area calculated from N_2 adsorption isotherm using BET equation.
[b] Pore volume (PV) calculated from N_2 uptake at $p/p_0 = 0.95$.
[c] Micro pore volume (MPV) calculated from N_2 uptake at $p/p_0 = 0.10$.

Noteworthy, when we analyzed P(3PT-F)-2, P(3PT-F)-3, and P(3PT-F)-4 before the purification step in the soxhlet apparatus, all samples exhibited a flake-like surface (see Figs. S6–S8). This indicates that the surface of P(3PT-F)-2 and P(3PT-F)-4 potentially still consisted of unreacted groups that were converted or eliminated by the purification step, thus forming a more smooth surface morphology afterwards. In contrast, the stoichiometry in the reaction mixture of P(3PT-F)-3 may lead to a more complete polymerization, thus retaining their initial morphology.

The particle size distribution after ultrasonication (Fig. 3i) matches the particle sizes visible in SEM imaging. All samples exhibit one peak at diameters around 350 nm and a bigger one with diameters of several µm. This indicates that the visible, µm-sized aggregates although made up of smaller particles are rigidly connected, as it was not split by ultrasonication in a bath for 30 min. The non-upscaled samples are also exhibiting a small peak between 100 µm and 500 µm due to even larger aggregates. This peak is missing in the upscaled synthesis, probably caused by a decrease in particle collisions due to a differing rheological behavior.

The particle size may be optimized with changes in polymerization temperature, dispersant amount or other synthesis parameters. Nonetheless, as this is the first publication about this polymer network, future research is needed to find optimal processing parameters. The use of organic solvents or surfactants, however, may again diminish the eco-friendly approach of this polymerization route as they often lead to unwanted contaminations [18,42,43].

To characterize the network structure and chemical composition of the polymers, solid-state NMR spectroscopy, ATR-FTIR spectroscopy, WAXS measurements and thermogravimetric analysis were carried out. Understanding the methylene and ether cross-linking as well as possible

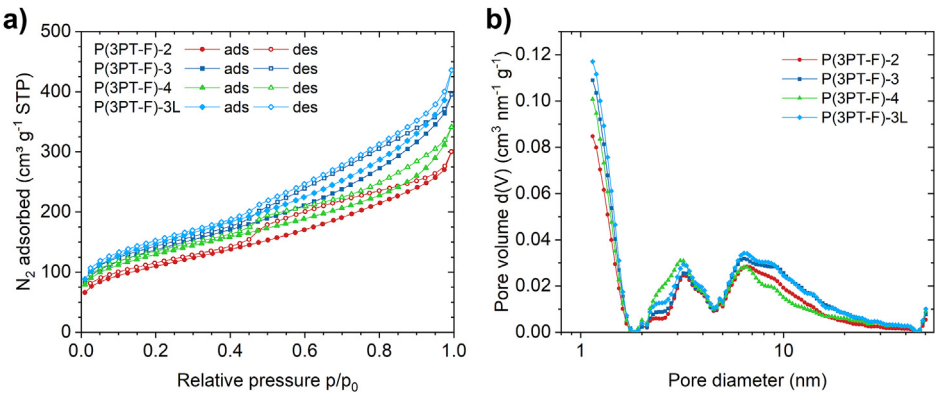

Fig. 2. a) Nitrogen (N_2) sorption isotherms measured at 77 K for the P(3PT-F) samples, b) Pore size distribution (PSD) analysis for the P(3PT-F) samples, calculated from the adsorption branch by using QSDFT (quenched solid-state density functional theory) model for carbon with slit/cylindrical/sphere pores. Data points in the adsorption and desorption branch of the isotherms are indicated by filled and empty symbols, respectively. P(3PT-F)-2 is shown in red with circles, P(3PT-F)-3 in dark blue with squares, P(3PT-F)-4 in green with triangles, and P(3PT-F)-3L in light blue with diamonds. Carbon dioxide (CO_2) sorption isotherms measured at 273 K are shown in Fig. S5. (For interpretation of the references to color in this figure legend, the reader is referred to the Web version of this article.)

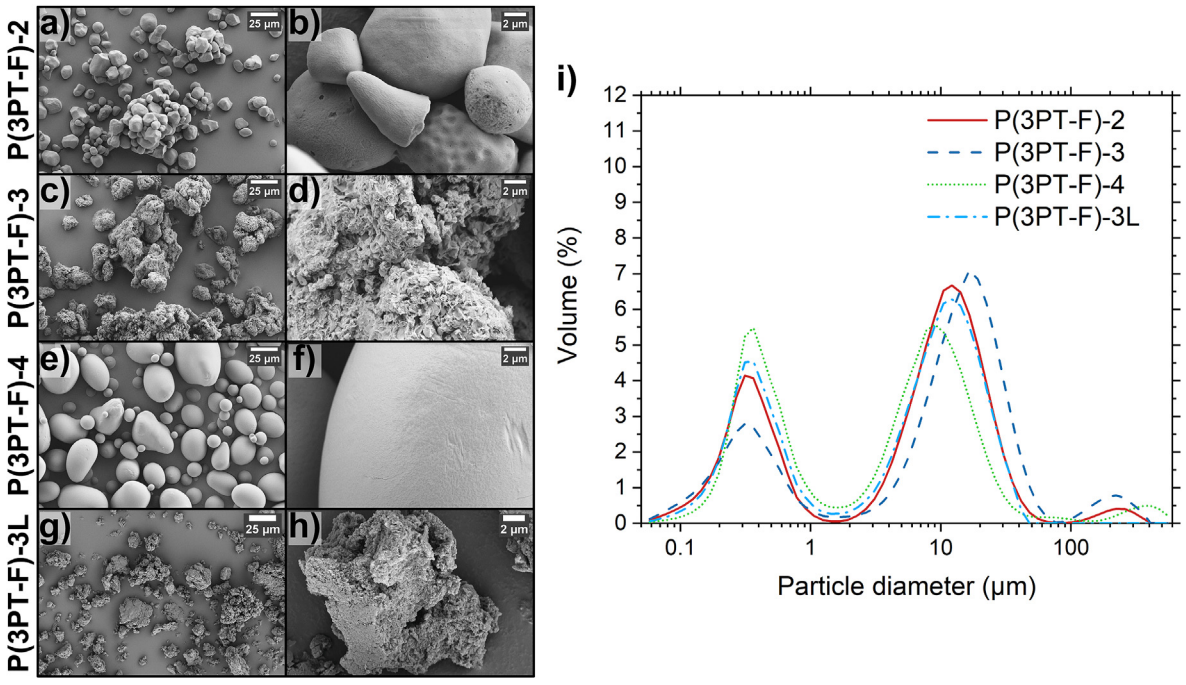

Fig. 3. SEM images of a) and b) P(3PT-F)-2, c) and d) P(3PT-F)-3, e) and f) P(3PT-F)-4, g) and h) P(3PT-F)-3L and i) particle size distribution (volume) for the samples with P(3PT-F)-2 in red (solid line), P(3PT-F)-3 in dark blue (dashed line), P(3PT-F)-4 in green (dotted line), and P(3PT-F)-3L in light blue (dash-dot line). (For interpretation of the references to color in this figure legend, the reader is referred to the Web version of this article.)

tautomerism are especially important for the understanding of the polymer network and its reactivity.

In the $^{13}C\{^{1}H\}$ CP-MAS spectra (stack plot in Fig. 4a), the methylene cross-linking is clearly observed as a broad peak around 10–30 ppm while the ether cross-linking is clearly observed as a broad peak around 50–70 ppm. Interpretation is obscured by peaks adjacent at 11 and 30 ppm for the methylene and 57 and 65 ppm for the ether, indicating multiple chemical environments with similar cross-linking maybe to tautomerized sub units.

With the high amount of heteroatoms in the aromatic sub structures, tautomerization of the hydroxyl group to a carbonyl group is visible. The corresponding carbonyl peak, expected around 206 ppm, is in fact greatly broadened, ranging from 180 to 220 ppm. While there are some differences, no clear identification of the potential tautomer is possible and both suggested tautomers (in ortho or para position to the triazine-linkage) are probable.

Fig. 4 and Table S1 show the dominant peak positions and a suggested assignment. Peak 1 at 11 ppm is due to methyl carbon on the tautomerized, former aromatic ring. The peaks 2 and 3 at 20 and 30 ppm are assigned to the methylene type cross-linking in two different environments, while the peak 4 at 61 ppm corresponds to ether type cross-linking. The 5th peak at 100 ppm is caused by protonated aromatic carbon, whereas peak 6 at 109 is assigned to aromatic carbon. Peak 7 at 167 ppm is due to phenol or azide aromatic carbon. Finally, the 8th peak at 197 ppm is assigned to the former aromatic carbon tautomerized to a carbonyl group. Fig. 4b shows a proposed sub structure of the polymer network.

Though CP-MAS spectra are not quantitative, trends within a series of samples investigated under identical conditions can be derived. Analysis of the CPMAS spectra was done by deconvolving each spectrum into 8 peaks using DMFit software [66]. The broad peak at 62 ppm, due to the ether type moiety, was deconvolved as a single peak as the signal-to-noise does not allow apparent peaks to be resolved individually. The small signal around 127 ppm could potentially be a spinning side band and was

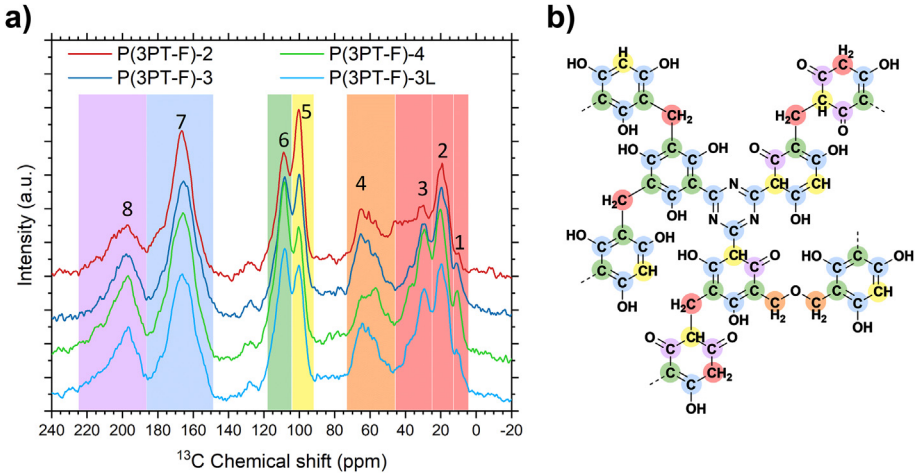

Fig. 4. a) ^{13}C CP MAS NMR spectra (stacked from bottom to top) for P(3PT-F)-2 (red line), P(3PT-F)-3 (dark blue line), P(3PT-F)-4 (green line) and P(3PT-F)-3L (light blue line) with peaks 1–8, described in detail in Table S1. The peaks are shaded according to the proposed assignments. b) Example chemical sub-structure of the polymer network. The colored highlights of the peaks 1–8 in a) correspond to the similarly highlighted carbon atoms in the chemical structure in b). (For interpretation of the references to color in this figure legend, the reader is referred to the Web version of this article.)

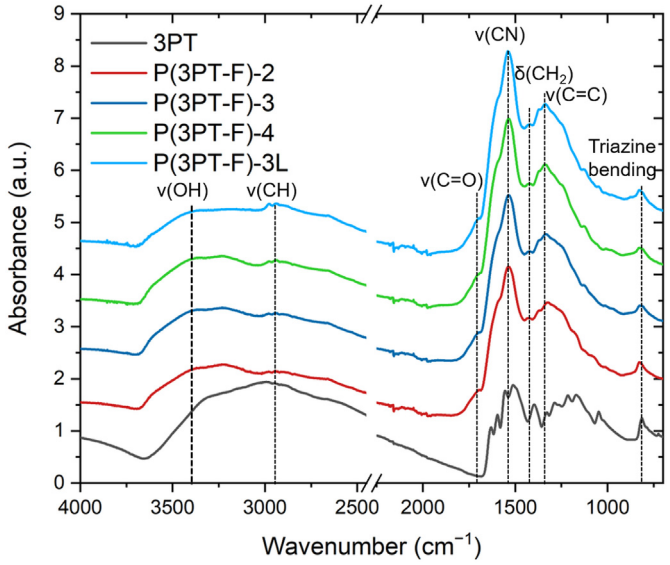

Fig. 5. ATR-FTIR spectrum (stacked from bottom to top) of 3PT (black), P(3PT-F)-2 (red), P(3PT-F)-3 (dark blue), P(3PT-F)-4 (green) and P(3PT-F)-3L (light blue) with the significant mode assignment and normalized to the *s*-triazine bending at 812 cm^{-1} for reasons of comparability. (For interpretation of the references to color in this figure legend, the reader is referred to the Web version of this article.)

not further analyzed. The relative content of the total integral for each peak is summarized in Table S1. Peaks 2 and 3 represent the methylene type cross-linking, while peak 4 represents the ether type cross-linking. Sample P(3PT-F)-3 shows a cross-linking ratio of 1.4:1 while the other three show a cross-linking ratio of 2:1. The linewidth in the ^{13}C CPMAS NMR spectra is considered to originate from inhomogeneous broadening, i.e. disorder in these materials.

The ATR-FTIR spectra are very similar despite the increase in formaldehyde equivalents (Fig. 5). All spectra were normalized to the *s*-triazine bending mode at 820 cm^{-1} to ensure comparability. The very broad ν(OH) mode is shifted towards a higher wavenumber (3390 cm^{-1}) when compared to the monomer 3PT (3340 cm^{-1}) presumably due to the inductive effect of methylene bridges. A further indicator for the network formation is the ν(CH) mode at 2980 cm^{-1} originating from the methylene linkages. The band at 1705 cm^{-1} originating from the ν(C═O) mode indicates, that the hydroxyl functionalities partially undergo the tautomerization to the carboxyl analogue in the network. Further observed modes are ν(CN) at 1543 cm^{-1}, δ (CH_2) at 1435 cm^{-1} and ν(C═C) at 1371 cm^{-1} and 1340 cm^{-1} that further support the formation of methylene bridges between the aromatic subunits [11,67].

From elemental analysis (see Table S2), a rough evaluation of the formaldehyde uptake per triazine and therefore cross-linking can be derived regarding the molar C/N ratio. The higher this value is, the more the sample is cross-linked. From direct comparison of P(3PT-F)-2, P(3PT-F)-3 and P(3PT-F)-4, it can be seen that the increased amount of paraformaldehyde also leads to a more cross-linked polymer.

From the TGA (see Figs. S3 and S4), two main decomposition steps under air atmosphere can be seen (after physical dehydration up to 120 °C): In the first step, approximately around 150 °C, both the monomer and the polymer show a mass loss that potentially corresponds to chemical dehydration from the hydroxyl groups. Also, as it is known from Poly(melamine-*co*-formaldehyde) networks, formaldehyde could be eliminated from ether bonds or non-cross-linked hydroxymethyl groups [68–70]. In the second, steeper step, beginning approximately at 300 °C, the complete decomposition of the network can be seen that is completed at 600 °C. In general, the samples exhibit a very similar behavior. However, under nitrogen atmosphere, this second decomposition step is less steep and levels off at around 600 °C, nearing a residual mass between 40 and 50 wt%. Hereby, potentially only the hydroxyl groups are decomposed while the aromatic and triazine structure may be preserved to a high percentage.

In WAXS measurements of the P(3PT-F) samples (see Fig. S9), a broad amorphous reflex with its maximum around 25.7° can be seen. This represents a shift towards lower 2Θ values, with respect to the monomer due to increased grid spacing between the 3PT units by cross-linking. The strong broadening of the reflex represents also a greater variance in this distance. In general, all P(3PT-F) samples show the same kind of amorphous reflexes with no detectable shift in the values of peak maxima. To investigate the surface properties of the P(3PT-F)-3L particles, their surface charge was determined in a streaming potential vs. pH measurement (see Fig. 6). It is visible that the particles exhibit a strong negative charge at between pH values of 3.5 and 9.0. This behavior is attributed to the hydroxyl groups of the polymer, easily deprotonated in water.

Although the pK_a values of 1,3,5-trihydroxy benzene are known to be around 8, 9 and 14 [71,72], the deprotonation of hydroxyl groups shown by the P(3PT-F)-3L sample is occurring at significantly lower pH. When adding 30 mg P(3PT-F)-3L to 30 mL ultrapure water (with $pH_{water} = 6.0$), the pH reduces to 4.0 after 24 h. This pH change can only be attributed to the hydroxyl groups as we have assured the purity of the 3PT monomer before polymerization by TGA, NMR, and elemental analysis. Here, complete absence of aluminum species was ensured. In the polymerization, no further reactants were used that could contribute to potential impurities as other functional groups or ions, which may influence the pH. The solid-state NMR is proving the chemical structure of the network formed. However, the strong tautomerism proven by solid-state NMR, the *s*-triazine ring of the monomer and increased mesomerism of the polymer must contribute towards a significantly lower pK_a and increased stabilization of its negative charge.

The highly negative surface charge of the particles, exhibited over the complete investigated pH range, grants a very good applicability of the particles for the adsorption of positively charged heavy metal ions.

3.2. Adsorption experiments with Ni^{2+}, Cd^{2+}, and Pb^{2+} onto P(3PT-F)-3L

For the adsorption study, P(3PT-F)-3L was used as adsorbent as it was easily producible in larger quantities and at the same time showing slightly better porosity. To demonstrate a potential application for the new polymer resin, adsorption experiments with lead, cadmium, and nickel ions as pollutants in water were investigated. Especially Pb^{2+},

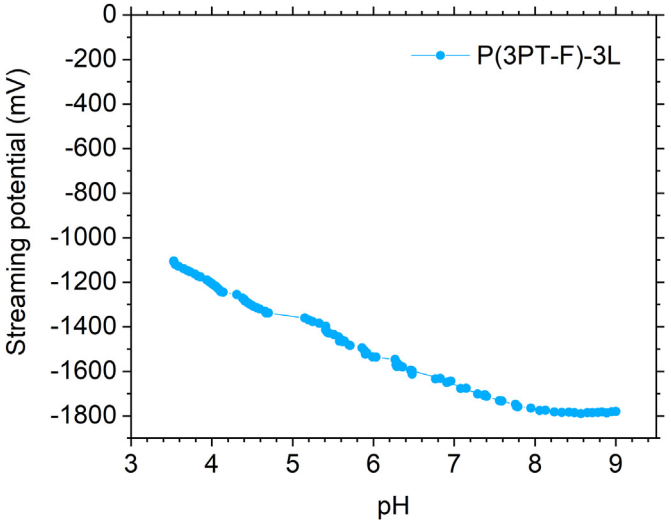

Fig. 6. Streaming potential of P(3PT-F)-3L (light blue) over the pH range of 3.5–9.0. (For interpretation of the references to color in this figure legend, the reader is referred to the Web version of this article.)

Cd^{2+}, and Ni^{2+} pose a high risk to both, humans [44,45,47–50,73–80] and various aquatic species [46,50,51,81,82] in extremely low concentrations. Therefore, we determined the adsorption isotherms of these elements over a broader concentration range to determine the efficiency in low concentrations as well as their capacity in high concentrations. An equilibration time of 24 h was chosen for these first experiments to ensure complete equilibration and mass transfer into the particles. The diffusion coefficients of all ions [83,84] should allow for mean diffusion length significantly higher than the particle diameters of P(3PT-F)-3L, which are all below 100 µm.

First, the transition metal ions Ni^{2+} and Cd^{2+} were tested with an adsorbent dose of 1 g/L (see Fig. 7a and b and Table 3). It is well visible for both experiments that in the low-concentration region, almost 100% of the respective ions was adsorbed, therefore c_{eq} is decreased to almost 0. Here, for initial Ni^{2+} concentrations of up to 1.6 mg/L, drinking water quality (limit value of 0.07 mg Ni/L, WHO [73]) can be achieved after adsorption as the pollution is reduced by two orders of magnitude. For higher concentrations of Ni^{2+}, a maximum experimental uptake up to 15 mg/g was achieved. This value is supported by the Langmuir and Sips isotherm model, whereas the Dubinin-Radushkevich fit potentially overestimates the maximum achievable uptake. Here, the Sips model as combination of the Langmuir and Freundlich isotherm was found to best represent the adsorption process, calculating a maximum adsorption capacity of 15.7 mg/g (corresponding to 268 µmol Ni^{2+}/g). Although the adsorption capacity Q_m of the Dubinin-Radushkevich model is less accurate, its activity coefficient β_{DR} is probably relatively accurately representing the slope of the isotherm (see Fig. S13). Here from, the mean free energy of adsorption $E_{Ads,DR}$ can be calculated via Eq. (9). It is visible that this energy is very high with a value of 17.3 kJ/mol leading to the assumption of a very strong interaction between the P(3PT-F)-3L particles and Ni^{2+}.

For Cd^{2+}, an initial concentrations of up to 0.13 mg/L is reduced to 0.005 mg/L, almost reaching drinking water quality (limit value of 0.003 mg Cd/L, WHO [73]). Cd^{2+} exhibits a higher plateau experimentally at 23 mg/g, also supported by the fitting with the Langmuir and Sips equations (Fig. 7b and S14). The Sips model, presenting the highest correlation, determines a maximum adsorption capacity of 23.6 mg/g (corresponding to 211 µmol/g) (see Table 3). This plateau is almost reached with an initial concentration of 50 mg/L Cd^{2+}, due to the extremely high affinity exhibited by the particles towards Cd^{2+}, represented also from the high $E_{Ads,DR}$ value of 17.2 kJ/mol determined by the Dubinin-Radushkevich fit.

Pb^{2+} as a main group element showed the highest adsorption capacity with a plateau at around 90 mg/g (see Fig. 7c and S15). Nonetheless, it showed an extremely steep rise in the adsorption isotherm in the low concentration region. Up to an initial concentration of 1 mg/L, drinking water quality is achieved after adsorption (limit value of 0.01 mg Pb/L, WHO [73]). In general, a decrease in Pb^{2+} concentration of one order of magnitude or even above for initial concentrations of 50 mg/L were determined that shows the efficient attainment of the maximum adsorption capacity for this material. The adsorption capacity is given with 89.8 mg/g (corresponding to 433 mmol/g) from the Sips fitting that shows a higher molar uptake of Pb^{2+} than the other investigated metal ions. In contrast to Ni^{2+} and Cd^{2+}, Pb^{2+} readily forms hydroxyl species like $[Pb(OH)]^+$ and $[Pb_4(OH)_4]^{4+}$ [85] that require less adsorption sides per Pb^{2+} ion, therefore contributing towards the significantly higher uptake of Pb^{2+}. This may also result in a slightly lower adsorption energy (15.8 kJ/mol), when compared to Ni^{2+} and Cd^{2+}, but with still represents a very strong interaction between Pb^{2+} and P(3PT-F)-3L in general.

To gain further information about the nature of the adsorption process, the loaded adsorbent material was also analyzed by SEM-EDX after the adsorption experiments where the plateau of adsorption capacity was reached (see Table S3 and Figs. S16–S21). The elemental surface composition derived from the EDX spectra were in the same range to the achieved adsorption capacities with 1.1 wt% Ni^{2+}, 9.8 wt% Cd^{2+} and 14.7 wt% Pb^{2+} (see Table S3). Here, the mass concentration of Cd^{2+} and Pb^{2+} on the surface is higher than the corresponding adsorption capacity, while Ni^{2+} show a slightly lower mass concentration than respective capacities. Therefore, we can conclude that Cd^{2+} and Pb^{2+} are probably adsorbed more to the outside of the particles while Ni^{2+} is taken up into the pore structure to a higher degree. Here, the significantly larger ionic radii of Pb^{2+} and Cd^{2+} compared to Ni^{2+} may inhibit entrance of the micropore structure [86].

In general, a homogeneous adsorption of all heavy metal ions over the visible adsorbent surface is apparent in the elemental mapping, validating the use of Langmuir and Langmuir-based isotherms such as the Sips model (Figs. S16–S21, it is noteworthy that the shadows in the mappings are mainly caused by the detector placement).

Comparing the achieved adsorption capacities to literature (Tables S4–S6), P(3PT-F)-3L is especially competitive for the adsorption of Cd^{2+} and Pb^{2+}. Here, P(3PT-F)-3L shows capacities as high as commercially available resins or further modified resinous adsorbents. In the case of Pb^{2+}, the new *s*-triazine-based phenolic adsorbent partially surpasses them. Thus, this first test of this newly synthesized polymer show a promising point for further development.

3.2.1. *pH dependence*

To further analyze the adsorption mechanism and dependence on the solution pH or the presence of other ions, further experiments were conducted with Pb^{2+} as it showed the best adsorption capacity of the investigated contaminants.

The evaluation of the adsorption at differing pH_0 values gives information about the adsorption mechanism, therefore we conducted experiments with 100 mg/L Pb^{2+} at pH_0 values of 2.0, 3.0, and 4.0 besides the native pH of the solution that was 4.96 (Fig. 8). Experiments with higher pH values were not conducted as partial hydrolysis of Pb^{2+} and subsequent precipitation is expected as shown in literature [87]. As expected from the adsorbents structure, the initial pH influences the

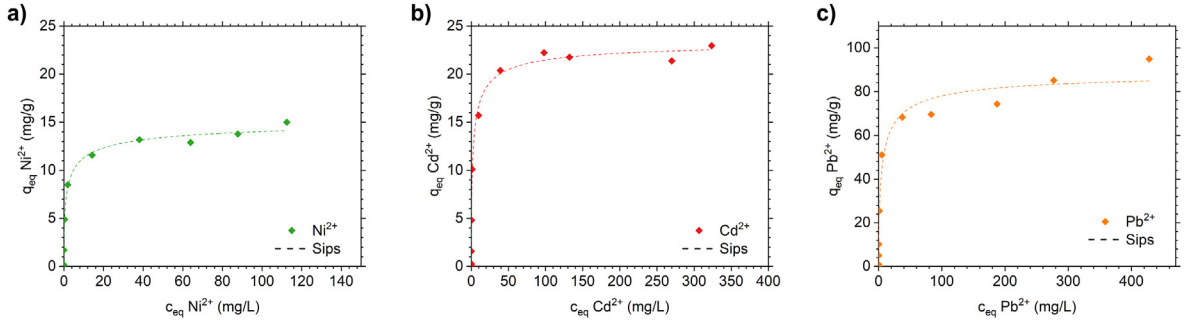

Fig. 7. Adsorption isotherm of a) Ni^{2+} from $NiSO_4$ solution and b) Cd^{2+} from $CdSO_4$ solution, and c) b) Pb^{2+} from $Pb(NO_3)_2$ solution onto P(3PT-F)-3L with the respective fittings for the Sips isotherm model. The pH values before and after adsorption are displayed in Figs. S10–S12. A graphical fitting comparison can be seen in Figs. S13–S15.

Table 3
Fitting parameters for Langmuir, Sips and Dubinin–Radushkevich isotherm models for adsorption of Ni^{2+}, Cd^{2+} and Pb^{2+} onto P(3PT-F)-3L. Q_m thereby is the maximum adsorption capacity, K is the equilibrium constant of Langmuir or Sips, n is the Sips model exponent, and β_{DR} represents the activity coefficient related to the mean free energy of adsorption $E_{Ads,DR}$. R^2 is the coefficient of determination (COD) for the respective fits. For all parameters, the corresponding standard error given from the fit are displayed. The respective graphical fitting comparison can be seen in Figs. S13–S15. The fitting for Dubinin-Radushkevich was conducted with concentration in mol/L.

Ion	Model	Q_m (mg/g)	K[a]	N	β_{DR} (10^{-9} mol^2/J^2)	$E_{Ads,DR}$ (kJ/mol)	R^2 (COD)
Ni^{2+}	Langmuir	13.5 ± 0.5	1.2 ± 0.36	–	–	–	0.966
	Sips	15.7 ± 1.1	0.79 ± 0.16	0.51 ± 0.08	–	–	0.991
	Dubinin– Radushkevich	22.2 ± 1.4	–	–	1.67 ± 0.17	17.3 ± 0.9	0.978
Cd^{2+}	Langmuir	21.7 ± 0.6	0.63 ± 0.13	–	–	–	0.986
	Sips	23.6 ± 0.8	0.57 ± 0.06	0.62 ± 0.06	–	–	0.996
	Dubinin– Radushkevich	34.8 ± 2.4	–	–	1.70 ± 0.19	17.2 ± 1.0	0.970
Pb^{2+}	Langmuir	81.1 ± 3.3	0.33 ± 0.09	–	–	–	0.970
	Sips	89.8 ± 7.4	0.34 ± 0.07	0.65 ± 0.14	–	–	0.978
	Dubinin–Radushkevich	149.3 ± 13.8	–	–	1.99 ± 0.24	15.8 ± 1.0	0.963

[a] Unit of K for Langmuir model is L/mg and for Sips model $(L/mg)^n$.

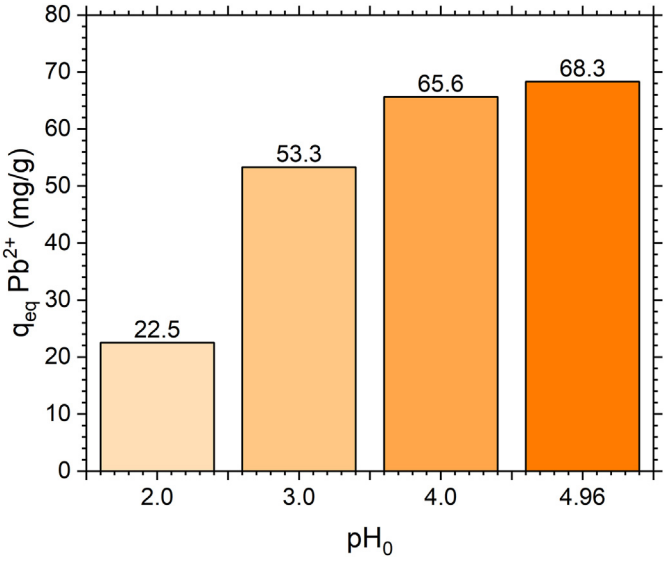

Fig. 8. Adsorption capacity of P(3PT-F)-3L from experiments with a $Pb(NO_3)_2$ solution with c_0 = 100 mg/L Pb^{2+} at various pH_0. The respective pH_{eq} values after adsorption are presented in Fig. S22.

adsorption performance of the P(3PT-F) sample. Lowering the pH, here leads to less adsorption of Pb^{2+}. At pH_0 = 2.0, an adsorption capacity of only 22.5 mg/g is achieved that directly is attributed to less deprotonation of the adsorbent's hydroxyl groups, thus less active binding sites present for the adsorption. Furthermore, the formation of Pb^{2+} hydroxyl complexes is inhibited, further decreasing the adsorption capacity as discussed in the previous section [85]. Nonetheless, even at these harsh conditions, a third of the adsorption performance is retained. As Pb^{2+} is most often present in low amounts, the retention of this contaminant is possible even at this pH value but with overall lower capacity. At a pH_0 of 3.0, 78% of the original adsorption capacity is achieved, showing the viability of the adsorbent. In addition, municipal wastewater exhibits often pH values close to neutral pH and even industrial wastewaters with high concentrations of metal ions seldom reach extremely low pH values [88–91].

3.2.2. Selectivity

To gain information about possible competitive adsorption influences, a separate experiment, where Pb^{2+} was adsorbed in the presence of other abundantly present ions in wastewaters, was conducted. Here, the ions K^+, Mg^{2+}, Ca^{2+}, Fe^{2+} and Cu^{2+} were chosen, each at a concentration of 0.5 mmol/L that is in the plateau region of the Pb^{2+} isotherm (corresponding to 100 mg/L Pb^{2+}) (Fig. 9). Here, all ions were used as their respective chloride salt as chloride also represents the most abundant natural anion. It is visible, that the P(3PT-F)-3L sample showed extremely strong adsorption of Cu^{2+} as well as Pb^{2+} that is not impaired by the presence of K^+, Mg^{2+}, Ca^{2+} and Fe^{2+} ions. Although the adsorption of Cu^{2+} is preferred over Pb^{2+} by means of molarity, the effective loading of Pb^{2+} is higher than Cu^{2+} (Fig. 9b). Often, Cu^{2+} is also regarded as harmful [92,93], thus separation via adsorption by P(3PT-F)-3L can be considered a benefit. To add to this, ions as Ca^{2+}, Mg^{2+}, Fe^{2+}, K^+ and Cl^- that occur more often in both municipal and industrial wastewaters than Cu^{2+}, only are adsorbed in a negligible amount. This shows that the interaction of P(3PT-F) towards metal ions, especially Pb^{2+}, is selective and not attributable only to the charge of the respectively adsorbed ions.

3.2.3. Recyclability

To show that P(3PT-F) is reusable, we included an experiment as proof of principle, in which the material first adsorbed Pb^{2+} from a 30 mL $Pb(NO_3)_2$ solution containing 100 mg/L Pb^{2+} for 24 h. Subsequently, we desorbed the loaded Pb^{2+} with 10 mL 0.5 M aqueous HCl (see Fig. 10). From the experiments, it is visible that the desorption step can be regarded as quantitative as the desorbed amount and the adsorbed amount are basically equal with the deviation likely to result from the multiple centrifugation and washing steps. The adsorption achieved during the second cycle leads to a very similar capacity as the first one, proving excellent reusability of the material. Here, for desorption only a third of the volume was used when comparing with the adsorptive solution as well as less time with 3 h for desorption vs. 24 h for adsorption. The 3 h diffusion time for the Pb^{2+}, which permeated the particles for 24 h before, was sufficient for complete extraction out of the particles again. This fact also shows that the equilibration time for the adsorption of Pb^{2+} can be lowered in future investigations.

Our experiments demonstrates also that desorption can be done with plain HCl circumventing the use of organic chelating agents such as ethylenediaminetetraacetic acid, increasing ecofriendliness of the process.

The adsorption experiments at differing pH_0 as well as the selectivity evaluation and the successful desorption via HCl also directly provide viable insight into the adsorption mechanism. It is apparent that the adsorption significantly depends on the deprotonation of the hydroxyl functionalities that increases with pH. However, selectivity experiments prove that adsorption is not solely dependent on the charge of the ions, we conclude that the *s*-triazine moiety facilitates the adsorption of Pb^{2+} and Cu^{2+} that are both well known for their coordinative chemistry [94]. Furthermore, iron ions that are prone to oxidize about the duration of the experiment, and thus should exhibit a positive charge of +III, are not adsorbed in considerable amounts. Therefore, the triazine moiety increases the interaction towards the tested ions, enhancing the adsorption.

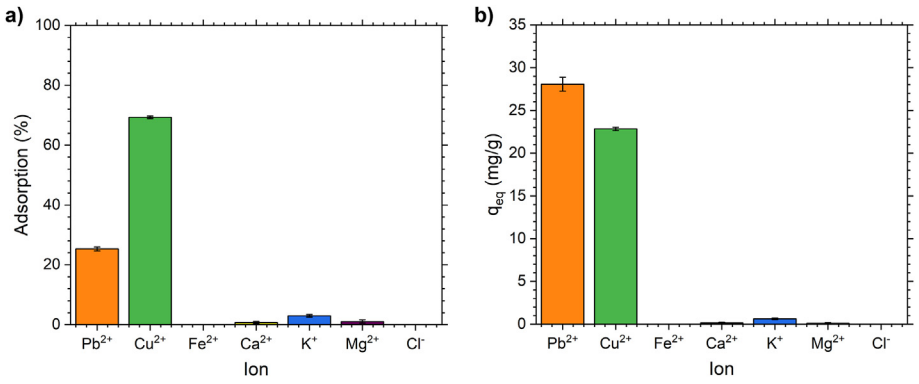

Fig. 9. a) Percentage adsorption and b) adsorption capacity of P(3PT-F)-3L from the selectivity experiments with a solution containing 0.5 mmol of Pb^{2+} (103.6 mg/L), Cu^{2+} (31.8 mg/L), Fe^{2+} (27.9 mg/L), Ca^{2+} (20.0 mg/L), K^{+} (19.6 mg/L), Mg^{2+} (12.2 mg/L), and the respective anion Cl^{-} of all ions with c_{0,Cl^-} = 3 mmol/L (212.7 mg/L). The experiment was conducted as triplet with respective standard deviation in both percentage adsorption and capacity shown as vertical bars. The pH_0 before adsorption was 4.01 and pH_{eq} after adsorption 3.02.

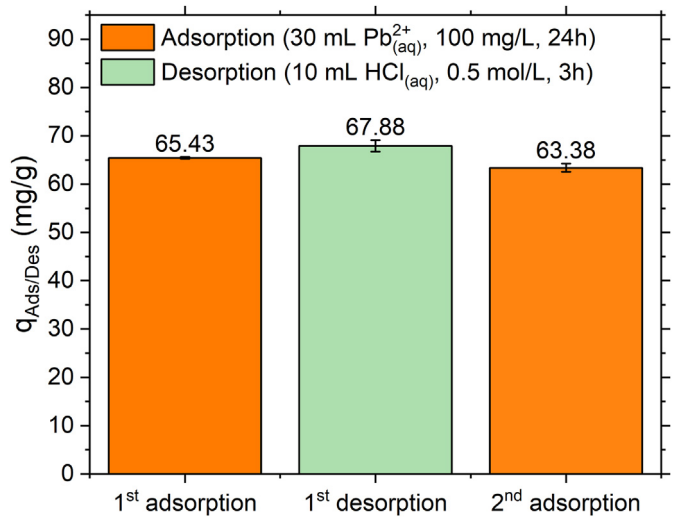

Fig. 10. Adsorbed (orange) and desorbed (green) capacity of Pb^{2+} from respective adsorption/desorption experiments of P(3PT-F)-3L. The error bars correspond to the standard deviation from duplets. Adsorption was carried out with 30 mL $Pb(NO_3)_2$ solution containing 100 mg/L Pb^{2+} with an equilibration time of 24 h. Desorption was carried out using 10 mL 0.5 M HCl solution for 3 h equilibration time. The capacity of Pb^{2+} that was ad-/desorbed, was calculated with respect to the total amount of Pb^{2+} in the respective 30 mL or 10 mL. The initial pH_0 of the adsorption experiments was 5.1 and pH_{eq} after adsorption was 3.3 for both times. (For interpretation of the references to color in this figure legend, the reader is referred to the Web version of this article.)

4. Conclusions

We presented the successful preparation of a previously unknown polymer for the application in heavy metal ion removal. In a facile dispersion polymerization using water as dispersant, a highly nanoporous polymer with specific surface areas up to 531 m^2/g were obtained. We thoroughly characterized its chemical composition elemental analysis and FTIR spectroscopy. The morphology and physicochemical properties of the material were evaluated in detail using electron microscopy, N_2 and CO_2 adsorption as well as particle size and streaming potential vs. pH measurements. With a successful upscaling, material for batch adsorption experiments was obtained in a more detailed investigation, the adsorption isotherms for Ni^{2+}, Cd^{2+}, and Pb^{2+} were determined. Here, maximum adsorption capacities of 16 mg Ni^{2+}/g, 24 mg Cd^{2+}/g, and 90 mg Pb^{2+}/g were attained. In realistically low concentrations, the heavy metal contamination was reduced by up to two orders of magnitude, thus achieving drinking water quality in these experiments. The high amount of hydroxyl and triazine functionalities of the polymer is enabling a very strong interaction with metal ions in terms of ionic interactions as well as coordinative bonds. In general, a very steep uptake in the adsorption isotherms was observed, also represented by the very high mean free energy of adsorption, calculated by fittings with the Dubinin-Radushkevich model. Our study shows that the polymer is especially viable because of its high affinity towards the analyzed metal ions leading to a high uptake already in low concentrations of the contaminants. Furthermore, our adsorbent shows outstanding capacities for the adsorption of Cd^{2+} and Pb^{2+}. Although the adsorption capacity decreases at lower pH_0 values, we could show that even at harsh conditions of $pH_0 = 2$, 33% of the capacity is retained, while for $pH_0 = 3.0$, 78% of the initial capacity can be achieved. From selectivity experiments, it was found that the abundant, significantly less toxic ions Ca^{2+}, Mg^{2+}, Fe^{2+}, K^{+} and Cl^{-} did not interfere, while the less common Cu^{2+} showed significant adsorption. Herein, Pb^{2+} still showed the highest adsorption capacity in terms of mass contaminant per mass adsorbent. With a short recycling experiment, we proved that desorption can be carried out easily using 0.5 M HCl in a low volume and at significantly less time than the adsorption (3 h vs. 24 h). Reusing the adsorbent a second time yielded in an unimpaired adsorption capacity for Pb^{2+}.

Overall, this could lead to further development of this new material and can exhibit an impact on the treatment of water to achieve safety in terms of drinking water quality demanded by the WHO.

Author contributions

Konstantin B. L. Borchert: Conceptualization, methodology, validation, formal analysis, investigation, data curation, writing – original draft preparation, writing – review & editing, visualization. **Christine Steinbach:** Investigation, validation, writing – review & editing. **Berthold Reis:** Investigation, validation, writing – review & editing. **Niklas Gerlach:** Investigation, validation, writing – review & editing. **Benjamin Kohn:** Investigation, validation, writing – review & editing. **Ulrich Scheler:** Investigation, validation, writing – review & editing. **Simona Schwarz:** Resources, writing – review & editing, supervision, project administration, funding acquisition. **Dana Schwarz:** Resources, supervision, project administration, funding acquisition.

Funding

This work was supported by the German Federal Ministry of Education and Research [grant number 01DJ18010].

Declaration of competing interest

The authors declare that they have no known competing financial interests or personal relationships that could have appeared to influence the work reported in this paper.

Data availability

Data will be made available on request.

Acknowledgments

The authors want to thank Eileen Schierz for the conduction of the elemental analysis.

Appendix A. Supplementary data

Supplementary data to this article can be found online at https://doi.org/10.1016/j.jciso.2022.100066.

References

[1] J. Huang, S.R. Turner, Hypercrosslinked polymers: a review, Polym. Rev. 58 (2018) 1–41.
[2] C. Wang, C. Li, E.R.C. Rutledge, S. Che, J. Lee, A.J. Kalin, C. Zhang, H.-C. Zhou, Z.-H. Guo, L. Fang, Aromatic porous polymer network membranes for organic solvent nanofiltration under extreme conditions, J. Mater. Chem. 8 (2020) 15891–15899.
[3] S. Nandi, U. Werner-Zwanziger, R. Vaidhyanathan, A triazine–resorcinol based porous polymer with polar pores and exceptional surface hydrophobicity showing CO 2 uptake under humid conditions, J. Mater. Chem. 3 (2015) 21116–21122.
[4] S. Nandi, J. Rother, D. Chakraborty, R. Maity, U. Werner-Zwanziger, R. Vaidhyanathan, Exceptionally stable Bakelite-type polymers for efficient pre-combustion CO 2 capture and H 2 purification, J. Mater. Chem. 5 (2017) 8431–8439.
[5] M. Saleh, S.B. Baek, H.M. Lee, K.S. Kim, Triazine-based microporous polymers for selective adsorption of CO 2, J. Phys. Chem. C 119 (2015) 5395–5402.
[6] J. Gu, P. Shao, L. Luo, Y. Wang, T. Zhao, C. Yang, P. Chen, F. Liu, Microporous triazine-based ionic hyper-crosslinked polymers for efficient and selective separation of H2S/CH4/N2, Separ. Purif. Technol. 285 (2022), 120377.
[7] K. Wang, H. Huang, D. Liu, C. Wang, J. Li, C. Zhong, Covalent triazine-based frameworks with ultramicropores and high nitrogen contents for highly selective CO2 capture, Environ. Sci. Technol. 50 (2016) 4869–4876.
[8] I.D. Wessely, A.M. Schade, S. Dey, A. Bhunia, A. Nuhnen, C. Janiak, S. Bräse, Covalent triazine frameworks based on the first pseudo-octahedral hexanitrile monomer via nitrile trimerization: synthesis, porosity, and CO2 gas sorption properties, Materials 14 (2021).
[9] N. Nouruzi, M. Dinari, N. Mokhtari, B. Gholipour, S. Rostamnia, S. Khaksar, R. Boluki, Porous triazine polymer: a novel catalyst for the three-component reaction, Appl. Organomet. Chem. 34 (2020) 153.
[10] D. Mullangi, S. Nandi, S. Shalini, S. Sreedhala, C.P. Vinod, R. Vaidhyanathan, Pd loaded amphiphilic COF as catalyst for multi-fold Heck reactions, C-C couplings and CO oxidation, Sci. Rep. 5 (2015), 10876.
[11] S. Nandi, V.M. Dhavale, S. Shalini, U. Werner-Zwanziger, H. Singh, S. Kurungot, R. Vaidhyanathan, Lithium-assisted proton conduction at 150 °C in a microporous triazine-phenol polymer, Adv. Mater. Interfac. 2 (2015), 1500301.
[12] Y. Wang, J. Xiao, H. Wang, T.C. Zhang, S. Yuan, N-doped porous carbon derived from solvent-free synthesis of cross-linked triazine polymers for simultaneously achieving CO2 capture and supercapacitors, Chemistry (Rajkot, India) 27 (2021) 7908–7914.
[13] R. Peng, G. Chen, F. Zhou, R. Man, J. Huang, Catalyst-free synthesis of triazine-based porous organic polymers for Hg2+ adsorptive removal from aqueous solution, Chem. Eng. J. 371 (2019) 260–266.
[14] Y. He, Q. Liu, F. Liu, C. Huang, C. Peng, Q. Yang, H. Wang, J. Hu, H. Liu, Porous organic polymer bifunctionalized with triazine and thiophene groups as a novel adsorbent for removing Cu (II), Microporous Mesoporous Mater. 233 (2016) 10–15.
[15] N. Mokhtari, M. Dinari, O. Rahmanian, Novel porous organic triazine-based polyimide with high nitrogen levels for highly efficient removal of Ni(II) from aqueous solution, Polym. Int. 68 (2019) 1178–1185.
[16] K.B.L. Borchert, C. Steinbach, B. Reis, N. Gerlach, P. Zimmermann, S. Schwarz, D. Schwarz, Mesoporous poly(melamine-co-formaldehyde) particles for efficient and selective phosphate and sulfate removal, Molecules 26 (2021) 6615.
[17] D. Schwarz, J. Weber, Organic-solvent free synthesis of mesoporous and narrow-dispersed melamine resin particles for water treatment applications, Polymer 155 (2018) 83–88.
[18] D. Schwarz, J. Weber, Synthesis of mesoporous poly(melamine-formaldehyde) particles by inverse emulsion polymerization, J. Colloid Interface Sci. 498 (2017) 335–342.
[19] T.J. Mooibroek, P. Gamez, The s-triazine ring, a remarkable unit to generate supramolecular interactions, Inorg. Chim. Acta. 360 (2007) 381–404.
[20] H. Shan, S. Li, Z. Yang, X. Zhang, Y. Zhuang, Q. Zhu, Di Cai, P. Qin, J. Baeyens, Triazine-based N-rich porous covalent organic polymer for the effective detection and removal of Hg (II) from an aqueous solution, Chem. Eng. J. 426 (2021), 130757.
[21] K.B.L. Borchert, K.H. Carrasco, C. Steinbach, B. Reis, N. Gerlach, M. Mayer, S. Schwarz, D. Schwarz, Tuning the pore structure of templated mesoporous poly(melamine-co-formaldehyde) particles toward diclofenac removal, J. Environ. Manag. 324 (2022), 116221, https://doi.org/10.1016/j.jenvman.2022.116221.
[22] F. Fu, Q. Wang, Removal of heavy metal ions from wastewaters: a review, J. Environ. Manag. 92 (2011) 407–418.
[23] E.O. Skogley, A. Dobermann, Synthetic ion-exchange resins: soil and environmental studies, J. Environ. Qual. 25 (1996) 13–24.
[24] T.A. Kurniawan, G.Y.S. Chan, W.-H. Lo, S. Babel, Physico–chemical treatment techniques for wastewater laden with heavy metals, Chem. Eng. J. 118 (2006) 83–98.
[25] S.K. Sahni, R. van Bennekom, J. Reedijk, A spectral study of transition-metal complexes on a chelating ion-exchange resin containing aminophosphonic acid groups, Polyhedron 4 (1985) 1643–1658.
[26] D.S. Stefan, I. Meghea, Mechanism of simultaneous removal of Ca2+, Ni2+, Pb2+ and Al3+ ions from aqueous solutions using Purolite® S930 ion exchange resin, Compt. Rendus Chem. 17 (2014) 496–502.
[27] B. Alyüz, S. Veli, Kinetics and equilibrium studies for the removal of nickel and zinc from aqueous solutions by ion exchange resins, J. Hazard Mater. 167 (2009) 482–488.
[28] H.P. Gregor, J.I. Bregman, Studies on ion-exchange resins. IV. Selectivity coefficients of various cation exchangers towards univalent cations, J. Colloid Sci. 6 (1951) 323–347.
[29] S.K. Samanta, B.M. Misra, Ion exchange selectivity of a resorcinol-fqrmaldehyde polycondensate resin for cesium in relation to other alkali metal ions, Solvent Extr. Ion Exch. 13 (1995) 575–589.
[30] R. Verma, P.K. Maji, S. Sarkar, Detailed investigation of effective trace Cr(VI) removal mechanism by anion exchange resin with phenol–formaldehyde matrix, J. Ind. Eng. Chem. 188 (2022) 276.
[31] S.A. Shady, Selectivity of cesium from fission radionuclides using resorcinol-formaldehyde and zirconyl-molybdopyrophosphate as ion-exchangers, J. Hazard Mater. 167 (2009) 947–952.
[32] V.I. Gorshkov, V.A. Ivanov, I.V. Staina, Selectivity of phenol–formaldehyde resins and separation of rare alkali metals, React. Funct. Polym. 38 (1998) 157–176.
[33] A.N. Nikoloski, K.-L. Ang, Review of the application of ion exchange resins for the recovery of platinum-group metals from hydrochloric acid solutions, Miner. Process. Extr. Metall. Rev. 35 (2014) 369–389.
[34] I.B. Rae, S. Pap, D. Svobodova, S.W. Gibb, Comparison of sustainable biosorbents and ion-exchange resins to remove Sr2+ from simulant nuclear wastewater: batch, dynamic and mechanism studies, Sci. Total Environ. 650 (2019) 2411–2422.
[35] N. Astrini, L. Anah, H.R. Haryadi, Adsorption of heavy metal ion from aqueous solution by using cellulose based hydrogel composite, Macromol. Symp. 353 (2015) 191–197.
[36] X. Gao, C. Guo, J. Hao, Z. Zhao, H. Long, M. Li, Adsorption of heavy metal ions by sodium alginate based adsorbent-a review and new perspectives, Int. J. Biol. Macromol. 164 (2020) 4423–4434.
[37] Y. Ge, Z. Li, Application of lignin and its derivatives in adsorption of heavy metal ions in water: a review, ACS Sustainable Chem. Eng. 6 (2018) 7181–7192.
[38] M. Ochi, J. Ida, T. Matsuyama, H. Yamamoto, Thermoresponsive-interpenetrating polymer network hydrogels for heavy metal ion recovery, J. Appl. Polym. Sci. 135 (2018), 46701.
[39] L.A. Shah, M. Khan, R. Javed, M. Sayed, M.S. Khan, A. Khan, M. Ullah, Superabsorbent polymer hydrogels with good thermal and mechanical properties for removal of selected heavy metal ions, J. Clean. Prod. 201 (2018) 78–87.
[40] V. Gómez-Ceballos, A. García-Córdoba, Z. Zapata-Benabithe, J. Velásquez, G. Quintana, Preparation of hyperbranched polymers from oxidized lignin modified with triazine for removal of heavy metals, Polym. Degrad. Stabil. 179 (2020), 109271.
[41] G. Conn, S. Eisler, Synthesis and intramolecular hydrogen bonding networks of 2,4,6-tri(o-hydroxyaryl)-1,3,5-triazines, Org. Lett. 13 (2011) 5080–5083.
[42] Y. Wang, Y. Xie, Y. Zhang, S. Tang, C. Guo, J. Wu, R. Lau, Anionic and cationic dyes adsorption on porous poly-melamine-formaldehyde polymer, Chem. Eng. Res. Des. 114 (2016) 258–267.
[43] G. Yang, H. Han, C. Du, Z. Luo, Y. Wang, Facile synthesis of melamine-based porous polymer networks and their application for removal of aqueous mercury ions, Polymer 51 (2010) 6193–6202.
[44] United Nations Environment Programme, Chemical Branch, DTIE, Final Review of Scientific Information on Lead - Version of December 2010, 2010.
[45] J. Godt, F. Scheidig, C. Grosse-Siestrup, V. Esche, P. Brandenburg, A. Reich, D.A. Groneberg, The toxicity of cadmium and resulting hazards for human health, J. Occup. Med. Toxicol. 1 (2006) 22.
[46] G. Pyle, P. Couture, Nickel, in: Homeostasis and Toxicology of Essential Metals, Elsevier, 2011, pp. 253–289.
[47] M. Jaishankar, T. Tseten, N. Anbalagan, B.B. Mathew, K.N. Beeregowda, Toxicity, mechanism and health effects of some heavy metals, Interdiscipl. Toxicol. 7 (2014) 60–72.
[48] H.S. Kim, Y.J. Kim, Y.R. Seo, An overview of carcinogenic heavy metal: molecular toxicity mechanism and prevention, Journal of cancer prevention 20 (2015) 232–240.
[49] Air Quality Guidelines for Europe, second ed., WHO, Regional Office for Europe, Copenhagen, 2000.
[50] H. Ali, E. Khan, Bioaccumulation of non-essential hazardous heavy metals and metalloids in freshwater fish. Risk to human health, Environ. Chem. Lett. 16 (2018) 903–917.
[51] T.I. Moiseenko, N.A. Gashkina, Biogeochemistry of cadmium: anthropogenic dispersion, bioaccumulation, and ecotoxicity, Geochem. Int. 56 (2018) 798–811.
[52] S. Brunauer, P.H. Emmett, E. Teller, Adsorption of gases in multimolecular layers, J. Am. Chem. Soc. 60 (1938) 309–319.
[53] M. Thommes, K. Kaneko, A.V. Neimark, J.P. Olivier, F. Rodriguez-Reinoso, J. Rouquerol, K.S.W. Sing, Physisorption of gases, with special reference to the

evaluation of surface area and pore size distribution (IUPAC Technical Report), Pure Appl. Chem. 87 (2015) 1051–1069.
[54] K.S.W. Sing, Reporting physisorption data for gas/solid systems: with special reference to the determination of surface area and porosity, Pure Appl. Chem. 54 (1982) 2201–2218.
[55] I. Langmuir, The constitution and fundamental properties of solids and liquids. Part I. Solids, J. Am. Chem. Soc. 38 (1916) 2221–2295.
[56] R. Sips, On the structure of a catalyst surface, J. Chem. Phys. 16 (1948) 490–495.
[57] M.M. Dubinin, The equation of the characteristic curve of activated charcoal, Proceedings of the USSR Academy of Sciences 55 (1947) 327–329.
[58] F. Togue Kamga, Modeling adsorption mechanism of paraquat onto Ayous (Triplochiton scleroxylon) wood sawdust, Appl. Water Sci. 9 (2019) 456.
[59] K.Y. Foo, B.H. Hameed, Insights into the modeling of adsorption isotherm systems, Chem. Eng. J. 156 (2010) 2–10.
[60] M.A. Al-Ghouti, D.A. Da'ana, Guidelines for the use and interpretation of adsorption isotherm models: a review, J. Hazard Mater. 393 (2020), 122383.
[61] X. Zhou, Correction to the calculation of Polanyi potential from Dubinnin-Rudushkevich equation, J. Hazard Mater. 384 (2020), 121101.
[62] T.A. Osmari, R. Gallon, M. Schwaab, E. Barbosa-Coutinho, J.B. Severo, J.C. Pinto, Statistical analysis of linear and non-linear regression for the estimation of adsorption isotherm parameters, Adsorpt. Sci. Technol. 31 (2013) 433–458.
[63] B. Subramanyam, A. Das, Linearised and non-linearised isotherm models optimization analysis by error functions and statistical means, Journal of environmental health science & engineering 12 (2014) 92.
[64] J. Wang, X. Guo, Adsorption isotherm models: classification, physical meaning, application and solving method, Chemosphere 258 (2020), 127279.
[65] C. Schlumberger, M. Thommes, Characterization of hierarchically ordered porous materials by physisorption and mercury porosimetry—a tutorial review, Adv. Mater. Interfac. 8 (2021), 2002181.
[66] D. Massiot, F. Fayon, M. Capron, I. King, S. Le Calvé, B. Alonso, J.-O. Durand, B. Bujoli, Z. Gan, G. Hoatson, Modelling one- and two-dimensional solid-state NMR spectra, Magn. Reson. Chem. 40 (2002) 70–76.
[67] G. Socrates, Infrared and Raman Characteristic Group Frequencies: Tables and Charts, third ed., John Wiley & Sons LTD, Chichester [etc., 2015.
[68] C. Devallencourt, J.M. Saiter, A. Fafet, E. Ubrich, Thermogravimetry/Fourier transform infrared coupling investigations to study the thermal stability of melamine formaldehyde resin, Thermochim. Acta 259 (1995) 143–151.
[69] D.J. Merline, S. Vukusic, A.A. Abdala, Melamine formaldehyde: curing studies and reaction mechanism, Polym. J. 45 (2013) 413–419.
[70] S. Ullah, M.A. Bustam, M. Nadeem, M.Y. Naz, W.L. Tan, A.M. Shariff, Synthesis and thermal degradation studies of melamine formaldehyde resins, TheScientificWorldJOURNAL 2014 (2014), 940502.
[71] J. Sunkel, H. Staude, Der Einfluß von Dissoziation und Substitution auf die physikalischen Eigenschaften von Dioxybenzolen. 2. Mitteilung: Elektronenspektren, Ber. Bunsen Ges. Phys. Chem. 73 (1969) 203–209.
[72] D. Wang, K. Hildenbrand, J. Leitich, H.-P. Schuchmann, C.v. Sonntag, pH-dependent tautomerism and pK a values of phloroglucinol (1,3,5-trihydroxybenzene), studied by 13 C NMR and UV spectroscopy, Z. Naturforsch. B Chem. Sci. 48 (1993) 478–482.
[73] World Health Organization, Guidelines for Drinking-Water Quality: First Addendum to the, third ed., vol. 1, 2006 recommendations, Geneva.
[74] E.M. Caravati, Medical Toxicology, third ed., Lippincott, Williams & Wilkins, Philadelphia, op, 2004.
[75] L.M. Cleveland, M.L. Minter, K.A. Cobb, A.A. Scott, V.F. German, Lead hazards for pregnant women and children: part 1: immigrants and the poor shoulder most of the burden of lead exposure in this country. Part 1 of a two-part article details how exposure happens, whom it affects, and the harm it can do, Am. J. Nurs. 108 (2008) 40–49, quiz 50.
[76] United Nations Environment Programme, Chemical Branch, DTIE, Final Review of Scientific Information on Lead - Version of December 2010, 2010.
[77] A. Hartwig, Cadmium and cancer, Metal ions in life sciences 11 (2013) 491–507.
[78] Seventh annual report on carcinogens, Environ. Health Perspect. 102 (1994) 739.
[79] K.K. Das, R.C. Reddy, I.B. Bagoji, S. Das, S. Bagali, L. Mullur, J.P. Khodnapur, M.S. Biradar, Primary concept of nickel toxicity - an overview, J. Basic Clin. Physiol. Pharmacol. 30 (2018) 141–152.
[80] G. Genchi, A. Carocci, G. Lauria, M.S. Sinicropi, A. Catalano, Nickel: human health and environmental toxicology, Int. J. Environ. Res. Publ. Health 17 (2020).
[81] B.G. Church, P.A. van Sprang, M.J. Chowdhury, D.K. DeForest, Updated species sensitivity distribution evaluations for acute and chronic lead toxicity to saltwater aquatic life, Environ. Toxicol. Chem. 36 (2017) 2974–2980.
[82] M.D. Pavlaki, M.J. Araújo, D.N. Cardoso, A.R.R. Silva, A. Cruz, S. Mendo, A.M.V.M. Soares, R. Calado, S. Loureiro, Ecotoxicity and genotoxicity of cadmium in different marine trophic levels, Environ. Pollut. 215 (2016) 203–212.
[83] H. Sato, M. Yui, H. Yoshikawa, Ionic diffusion coefficients of Cs + Pb 2+ Sm 3+ Ni 2+ SeO 2-4 and TcO −4 in free water determined from conductivity measurements, J. Nucl. Sci. Technol. 33 (1996) 950–955.
[84] A.H. Shiva, P.R. Teasdale, W.W. Bennett, D.T. Welsh, A systematic determination of diffusion coefficients of trace elements in open and restricted diffusive layers used by the diffusive gradients in a thin film technique, Anal. Chim. Acta 888 (2015) 146–154.
[85] B.C. Bunker, W.H. Casey, The hydrolysis products: soluble multi-cation clusters, in: B.C. Bunker, W.H. Casey (Eds.), The Aqueous Chemistry of Oxides, Oxford University Press, 2016.
[86] I. Persson, Hydrated metal ions in aqueous solution: how regular are their structures? Pure Appl. Chem. 82 (2010) 1901–1917.
[87] M. Businelli, F. Casciari, D. Businelli, G. Gigliotti, Mechanisms of Pb (II) sorption and desorption at some clays and goethite-water interfaces, Agronomie 23 (2003) 219–225.
[88] A. Alsulaili, B.Y. Al-Buloushi, M.F. Hamoda, Seasonal variation pattern of physicochemical and microbial parameters in a wastewater treatment plant, DWT 208 (2020) 244–260.
[89] J. Wang, C.P. Huang, H.E. Allen, Predicting metals partitioning in wastewater treatment plant influents, Water Res. 40 (2006) 1333–1340.
[90] T. Li, W. Dong, Q. Zhang, D. Xing, W. Ai, T. Liu, Phosphate removal from industrial wastewater through in-situ Fe2+ oxidation induced homogenous precipitation: different oxidation approaches at wide-ranged pH, J. Environ. Manag. 255 (2020), 109849.
[91] G. Macchi, M. Pagano, M. Santori, G. Tiravanti, Battery industry wastewater: Pb removal and produced sludge, Water Res. 27 (1993) 1511–1518.
[92] B. Fjällborg, G. Dave, Toxicity of copper in sewage sludge, Environ. Int. 28 (2003) 761–769.
[93] V. Ochoa-Herrera, G. León, Q. Banihani, J.A. Field, R. Sierra-Alvarez, Toxicity of copper(II) ions to microorganisms in biological wastewater treatment systems, Sci. Total Environ. 412–413 (2011) 380–385.
[94] R.G. Pearson, Hard and soft acids and bases, J. Am. Chem. Soc. 85 (1963) 3533–3539.